AFGL 5157 NH$_3$: a new stellar cluster in the forming process *

Zhi-Bo Jiang[1,2], Zhi-Wei Chen[1,2,3], Yuan Wang[1,2], Ji Yang[1], Jia-Sheng Huang[4],

Qi-Zhou Zhang[4] and Giovani Fazio[4]

[1] Purple Mountain Observatory, Chinese Academy of Sciences, Nanjing 210008, China;
   zbjiang@pmo.ac.cn
[2] Key Laboratory of Radio Astronomy, Chinese Academy of Sciences, Nanjing 210008, China
[3] Graduate University of Chinese Academy of Sciences, Beijing 100049, China
[4] Harvard-Smithsonian Center for Astrophysics, 60 Garden Street, Cambridge, MA 02138, USA

Abstract We present the analysis of Spitzer/IRAC and near infrared imaging observation of AFGL 5157, an active star forming region. In the IRAC images, this region shows strong emissions of polycyclic aromatic hydrocarbons in channel 4 and emissions of H$_2$ in channel 2. Many of the H$_2$ features are aligned to form jet-like structures. Three bipolar jets in the NH$_3$ core region and a couple of jets northwest of the core have been identified. We identify the possible driving agents of the bipolar jets and show them to be very young. An embedded cluster has been detected in the NH$_3$ core; many members in the cluster have spectral energy distributions that increase from *JHK* bands toward longer wavelengths, indicative of their early evolutionary stages. Millimeter and submillimeter continuum emissions in the NH$_3$ core and the northwest subregion are found to coincide spatially with these presumable Class 0/I sources. The existence of H$_2$ bipolar jets and very young stellar objects suggests that star formation is continuing at the present epoch in these subregions. Combining information from previous studies, we propose a sequential star formation scenario in the whole AFGL 5157 region.

Key words: ISM: individual (AFGL 5157) — ISM: jets and outflows — ISM: lines and bands — stars: formation

1 INTRODUCTION

AFGL 5157 is an active star forming region that has recently attracted a great deal of attention. Near infrared (NIR) observations show that it is a cluster having tens of young stars (perhaps pre-main sequence stars) with a total mass of $\sim 100\,M_\odot$ that are just emerging out of their natal cloud (Chen et al. 1999; Kumar et al. 2006, hereafter NIR cluster). An IRAS point source (05345+3157) is associated with the brightest NIR source in the NIR cluster, IRS 1. The far infrared luminosity of the IRAS source is estimated to be $\sim 5.5 \times 10^3\,L_\odot$ at a distance of 1.8 kpc (Snell et al. 1988), and this value could be scaled up if the recent kinematical distance of 2.1 kpc is adopted (Molinari et al. 2008).

More interesting is the region $\sim 1.5'$ to the northeast of the NIR cluster. NH_3 emission lines were first reported by Torrelles et al. (1992) and we refer to this region as the NH_3 core hereafter. A number of molecules tracing high density gas, such as HCN (Pirogov 1999), N_2H^+ and N_2D^+ (Fontani et al. 2008), have been detected recently. Millimeter (mm) continuum peaks have been detected in the core region extending to the south (Klein et al. 2005). A molecular outflow was reported in the east-west direction (Snell et al. 1988; Zhang et al. 2005), which has been resolved by observations from the Submillimeter Array (SMA) into several outflows with a complex morphology (Fontani et al. 2009). A number of shocked H_2 emission knots have been detected (Chen et al. 2003). Some of them are associated with the Herbig–Haro (HH) objects (Torrelles et al. 1992) and the outflows. These shocked H_2 emission knots, although widespread and oriented towards different directions, show strong signs that they are associated with the NH_3 core, suggesting the presence of a protostellar cluster with ongoing star formation inside. However, few NIR sources have been found in the region, suggesting that this proto-cluster is still deeply embedded in its nursery. We therefore carried out an observation using the Spitzer Space Telescope (SST) to investigate the embedded population and its properties.

The observation reveals a large amount of deeply embedded sources that are not detected by Chen et al. (1999) in the NH_3 core, and a number of H_2 emission knots associated with the deeply embedded cluster. In this paper we present the highlights of the study.

2 OBSERVATIONS AND DATA REDUCTION

The observation was carried out on 2009 April 22, with IRAC mounted on the SST in imaging mode. Data in four channels (with central wavelengths 3.6, 4.5, 5.8 and 8.0 μm, hereafter ch1, ch2, ch3 and ch4, respectively) were obtained. For each channel, a total of 288 frames was taken, each having an effective exposure time of 10.4 s. After rejecting unusable frames (~ 30 frames in each channel), sets of basic calibration data that have also been corrected were used to make the mosaic of images using the software Mopex. Standard parameter inputs were used except for the pixel scale of the fiducial image, which was set to $0.72''$ per pixel, in order to obtain higher photometric accuracy. The final mosaic of images has ~ 40 min integration time resulting in a 5σ detection limit of ~ 0.1 mJy in all channels.

The aperture photometry was carried out using the DAOFIND and PHOT tasks in the IRAF software package. Since the core region is rather densely populated with point sources, we adopted 4 pixels ($2.88''$) as the aperture radius to do the aperture photometry. The fluxes were then corrected to 10 pixels ($7.2''$) in ch1 and ch2, and to 15 pixels ($10.8''$) in ch3 and ch4 because of the larger expected point-spread-function in these two channels. The correction factors were obtained by comparing the fluxes of stars in the reference fields, which were observed simultaneously with the targets in each channel, between the two apertures (i.e., $2.88''$ and $7.2''$ in ch1 and ch2, and $2.88''$ and $10.8''$ in ch3 and ch4, respectively). The final factors are 1.21, 1.21, 1.38 and 1.42 for the four channels, respectively, with uncertainties better than 10%. The corrected photometric data were then combined with the 2MASS point source catalog to obtain the spectral energy distributions (SEDs) of young stellar objects (YSOs) in the field.

3 RESULTS AND DISCUSSIONS

Figure 1 presents a pseudo-color image composed of ch1, ch3 and ch4 (top panel) and ch1, ch2 and ch3 (bottom panel) frames, with blue corresponding to the shortest wavelength and red to the longest. In the top panel, strong red extended emission is seen in the whole region, roughly extending from the southwest to the northeast, indicative of the existence of polycyclic aromatic hydrocarbon (PAH) molecules. A shell-like structure surrounding the NIR cluster (Chen et al. 1999) is clearly seen. Note that the feature forming a line from the north to south might be artifacts caused by the strong emission associated with the shell structure. We indicate them with arrows in the top panel. To the northeast
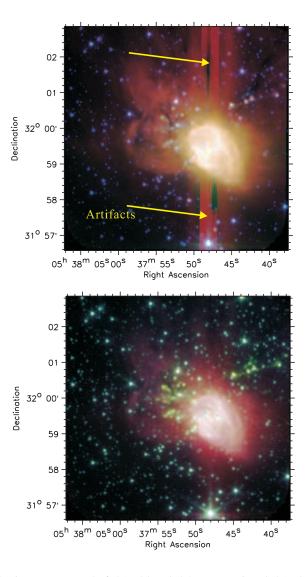
Fig. 1 Pseudo-color image composed of ch1, ch3 and ch4 (*top panel*) and ch1, ch2 and ch3 (*bottom panel*) images, with the red, green and blue corresponding to decreasing wavelengths. The R.A. and Dec. are given in J2000.0.

of the shell structure, in the NH_3 core region, diffuse emission features are highly structured, similar to the area associated with M17 (Povich et al. 2007) and other star forming regions (e.g. AFGL 437 Kumar Dewangan & Anandarao 2010). However, despite careful inspection we have not found a sharp edge associated with the PAH emission like in the case of M17 (Povich et al. 2007). This suggests that the AFGL 5157 area lacks very high-mass stars (e.g., O stars), and thus does not have extreme-ultraviolet photons to destroy the PAH molecules.

In the bottom panel, extended emissions are also obvious, similar to the top panel. In the NH_3 core region (Torrelles et al. 1992), a number of red point sources are detected. Many of them are not detected in the K_s-band or shorter wavelengths by 2MASS data or by Chen et al. (1999), suggesting
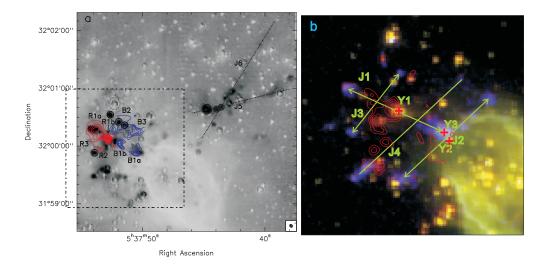
Fig. 2 (a) ch2/ch1 image in a smaller field than that of Fig. 1. Some point sources having stronger emission in ch2 than in ch1 are shown by black circles for reference. The contours are integrated intensity of the redshifted (red, $-9.2 \sim 6.4$ km s^{-1}) and blue shifted (blue, $-46.4 \sim -26.0$ km s^{-1}) components of CO $J = 2 - 1$ line emission observed with SMA (Fontani et al. 2009). The contour starts from 4σ (rms) with a step of 4σ (red: ~ 7.2 Jy beam^{-1} km s^{-1}; blue: ~ 6.0 Jy beam^{-1} km s^{-1}). The dashed square represents the field of (b). (b) Color image composed from ch2 (*red*), ch1(*green*) and the H$_2$ narrow band (*blue*) images. The H$_2$ narrow band (2.12 μm) image is adopted from Chen et al. (2003). The red contours are the 3 mm continuum observed by Fontani et al. (2009). The green arrows and lines denote the rough direction of the bipolar jets in the area. The red pluses indicate the position of YSOs mentioned in the text.

that they are still deeply embedded. The most prominent features are the compact and extended emissions in ch2, which appear green in the figure, generally close to the NH$_3$ core region. These objects, commonly referred to as extended or compact green objects, are likely shocked H$_2$ emission (Cyganowski et al. 2008) arising from the star forming activities.

3.1 The H$_2$ jets and Knots

To highlight the H$_2$ emission features, in Figure 2(a) we present the ch2/ch1 image, which is shown in a smaller field of view than that of Figure 1. Although the ch2/ch1 image can protrude the H$_2$ emission features, some point sources that show stronger continuum emissions in ch2 than in ch1 cannot be completely removed. These point-like sources are shown by black circles in the figure. For comparison, we overlay line wing emissions of CO $J = 2 - 1$ observed with the SMA. The red and blue contours are integrated intensities over velocity intervals (–9.2, 6.4) km s^{-1} and (–46.4, –26.0) km s^{-1}, similar to what is presented by Fontani et al. (2009).

Figure 2(a) reveals a large number of H$_2$ emission knots in the NH$_3$ core region and in the region $\sim 2'$ west. In the NH$_3$ core region, the H$_2$ emission features are very complex. The fact that tens of embedded YSOs exist in the region further complicates the picture. To identify these H$_2$ knots more concretely, in Figure 2(b) we present a color image composed from ch2 (red), ch1(green) and the H$_2$ (2.12 μm) narrow band (blue) images. The image of the H$_2$ narrow band is adopted from Chen et al. (2003). In this figure, the H$_2$ emission features are clearly seen in purple. By careful inspection, we
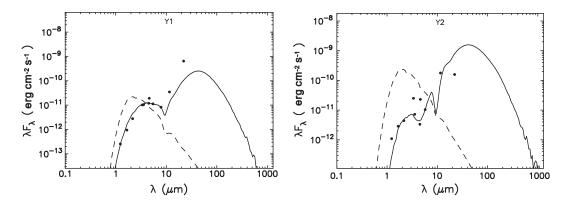
Fig. 3 Best fitting models for the two YSOs, Y1 (*left panel*) and Y2 (*right panel*). The filled circles show the input fluxes. The solid line shows the best fits. The dashed line shows the stellar photosphere corresponding to the central source of the best fitting model, as it would look in the absence of circumstellar dust (but including interstellar extinction).

could identify three bipolar structures and also a jet-like feature. Presumably they are jets arising from protostellar objects in the NH₃ core.

In the most prominent jet labeled J1, two bow shocks are seen in the two terminations, with their openings opposite to each other. At the midpoint of J1, a point source is detected in all four channels as well as in the JHK_s bands by 2MASS, being located at Y1: $05^h37^m52.02^s$, $+32°00'04.1''$ (J2000). The red and blue shifted CO components (R1, B1, Fig. 2(a)) are certainly associated with J1. R1 has two peaks: one coincides with the northeast H₂ bow shock (R1a), the other is near Y1 (R1b). Its blueshifted counterpart B1 splits into several parts, denoted as B1a and B1b. Inspection of the CO channel maps indicates that R1b, B1a and B1b are high velocity components ($\sim \pm 25$ km s^{-1} with respect to the system velocity ~ -19 km s^{-1}), while R1a has a lower velocity ($\sim +15$ km s^{-1}). Remarkably, B1a, which is also split into two parts, is located in the wake of the western H₂ bow shock of J1, suggesting that the CO outflow is entrained by J1 (Canto & Raga 1991; Raga & Cabrit 1993). The Wide-field Infrared Survey Explorer (WISE) archive image of the field shows a very strong mid-infrared point source at the Y1 position, suggesting that this object is very young. Using the photometric data including the J-band, ch4 and WISE point source photometry[1], we fit the SED to the YSO models given by Robitaille et al. (2007)[2]. The ten best fits give a mass of 2–5 $M_\odot$ and an age of 1.5 yr–3.5×10^5 yr.

Figure 3 shows the result of the best fit. We notice the strong excess emissions toward wavelengths longer than 10 µm. This is likely caused by contamination of other sources or interstellar dust emission since the FWHM of Y1 in the fourth band (22 µm) of WISE is as large as 20''. We also estimate the dynamical age by assuming a jet velocity of 25 km s^{-1} (the velocity of B1a) and an inclination angle of $\sim 60°$, resulting in an age of 2.2×10^4 yr at an assumed distance of 2.1 kpc (Molinari et al. 2008). We note, however, that the inclination angle is rather arbitrary, so we cannot estimate the error arising from the assumption. The only conclusion from the estimation of the dynamical age is that the driving source is quite young, consistent with the result from SED fitting.

The second bipolar jet (J2) is inferred from the bow shock at the northwest terminal and some faint H₂ emission knots in the pathway. At the southeast terminal, the morphology is irregular, probably due to the contamination of point sources, but we still notice a slight elongation in the jet direc-

---

[1] The online fitting tools can be accessed at *http://caravan.astro.wisc.edu/protostars/*.

[2] The WISE catalog can be found at *http://irsa.ipac.caltech.edu/Missions/wise.html*.

tion. In the middle of J2, there are two point sources, located at Y2: $05^h37^m49.83^s$, $+31°59'48.2''$ and Y3: $05^h37^m50.02^s$, $+31°59'52.4''$, respectively. The positional alignment with respect to the jet cannot suggest which one is the driving source. We then compute the SED fittings to these two objects. The best fits suggest that both Y2 and Y3 are massive YSOs of $\sim 8M_\odot$, but Y2 is much younger ($\sim 1.6 \times 10^4$ yr) than Y3 ($\sim 3.8 \times 10^6$ yr).

Figure 3 (right panel) shows the best fit for Y2. Since the point source detected by WISE is positionally associated with both Y2 and Y3, we assign the fluxes in four bands to Y2, while keeping in mind that they could be the combined contribution of both sources. This result would suggest Y2 is more likely the driving source of J2. We have not found any high velocity CO component associated with J2, probably because it is near the edge of the SMA field of view.

The third bipolar jet (J3) has a bow shock structure in the southeast and some faint tails in the northwest (Chen et al. 2003). The red and blue shifted CO emissions (R2, B2) are also detected along it (Fig. 2(a)). B2 is spatially coincident with the northwest H_2 knot and R2 is a little closer in terms of projection than the southeastern bow shock. The CO channel maps suggest R2 and B2 have velocities $\sim \pm 15$ km s^{-1}. Between the two ends, no point source is detected in the infrared. Fontani et al. (2008, 2009) observed this region with the SMA and Plateau de Bure Interferometer. In their 1 mm and 3 mm continuum images, there is a faint peak northeast of C1, which is also associated with the southern part of the northern N_2H^+ condensation. As can be seen in Figure 2(b), the faint peak is in the middle of J3. This mm source is probably the driving source of J3. Assuming a shock velocity of 15 km s^{-1} (the velocity of R2 and B2) and an inclination angle of $\sim 60°$, the dynamical age of this jet is estimated to be $\sim 1.8 \times 10^4$ yr.

Apart from the three bipolar jets, another jet-like knot (J4) is located between J2 and J3, elongated in the direction similar to that of J2. Faint H_2 emission features have been detected in ch2 as well as in the NIR (Chen et al. 2003). However, we have not found any point source along the path. At present, it is not possible to conclude where this jet has originated. A possible interpretation is that it is a parsec-scale jet from the northwest region. In addition, there are a number of faint H_2 emission features. They are distributed so disorderedly that we cannot currently tell from where they originate. Notably, there is likely another bipolar CO outflow with velocity $\sim \pm 15$ km s^{-1} (denoted as R3, B3) in the region, and R3 is contaminated by R1 and B3 is positionally connected to B2.

In the northwest region, two jet-like structures are found. One is stronger, roughly in the east-west direction. Some knots have also been detected by Chen et al. (2003). The other fainter jet feature, oriented in the southeast-northwest direction, is not detected by Chen et al. (2003). These two jets have a number of components that are too faint to determine their exact direction, so we only place two dotted lines along these components for illustration. Nevertheless, they are likely to have originated from the region where they intersect, and where a number of point sources with red SEDs are detected. These red point sources are reasonable candidates for the driving sources of the two jets. High-resolution observations of molecular outflows from this region may help us to understand the star forming activity there. In conclusion, the existence of jets/outflows in these subregions signals ongoing star formation in the NH_3 core and northwest region.

3.2 Distribution of the Young Population

In the entire field, a total of 480 point sources are detected in at least four bands (including 2MASS JHK_s bands). Using the combined photometric data, we construct the SEDs of the sources, which can help us to select local members from field stars. To do this, we classify the SEDs into six categories: (1) SEDs increasing monotonically towards longer wavelengths; (2) those having double peaks; (3) those with a single peak at K_s or longer wavelengths; (4) those with a single peak at H; (5) those decreasing monotonically towards longer wavelengths; (6) irregular SEDs. Figure 4 shows some example SEDs of the above categories except for Type 6.
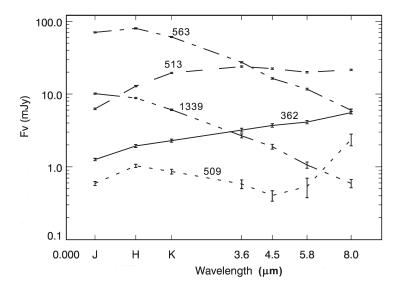
Fig. 4 Typical SEDs of the five categories. The numbers correspond to our internal photometric identifications. The sources, Nos. 362, 509, 513, 563 and 1339, show typical SED types 1–5, respectively. We note, however, that not all sources are detected in all bands like the examples shown here.

According to the theory of star formation, the categories would represent an evolutionary sequence from 1 to 5. Even considering the extinction drops from the J-band through ch4, Type 1 SEDs (66/480) should peak at ch1 or longer wavelengths, so they might be Class I YSOs or still earlier; Type 2 SED sources (35/480) could be Class I or II objects with the presence of disks. Type 3 SEDs (108/480) are probably T Tauri objects with weak disk emissions; Type 4 SEDs (135/480) are more evolved, but could still be YSOs with infrared color excesses; Type 5 SEDs (35/480) may be local YSOs or field stars. For the last category, the measured fluxes are generally small with large error bars. They might be YSOs or may be some line-emitting knots such as H$_2$, PAH features, field stars or even false-detections. We cannot infer their properties so we ignore this kind of detection in the following analysis.

Figure 5 shows the color-color diagram of the point sources detected in all four channels. It is not surprising to see that Type 1 sources are located in the Class 0/I block or in the upper-right corner of the Class II block. Type 2 sources are in the Class II block while Type 3 sources are in the Class II and III blocks. Type 4 and 5 sources are mostly in the Class III block. Such a coincidence indicates that the scheme of evolutionary sequence we proposed above is somewhat equivalent to the Class I–III sequence. We note here that it is difficult to state the virtues of one scheme over the other. Our proposed scheme contains information between 1 and 10 μm, while the color-color plot gives a more accurate color index in a smaller wavelength range.

To illustrate the distribution of the YSOs in the region, we make a pseudo-color image as follows: we use red points to denote the location where Type 1 SED YSOs are located; the same procedures are done for other types while Type 2 and 3 YSOs are marked by yellow points, Type 4 by green points, and Type 5 by blue points. Such an image is then convolved with a 45″×45″ kernel. The resultant image is presented in Figure 6.

As expected, the red areas, representing the youngest population that has so far been detected, are located in the NH$_3$ core, stretching southward along the edge of the shell-like structure surrounding the NIR cluster. Another red peak is located in the northwest region where two H$_2$ jets are found.
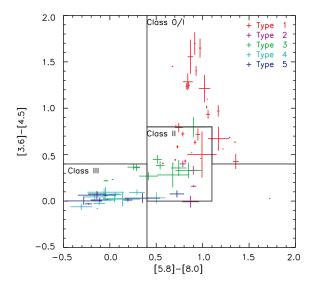
Fig. 5 The [5.8]–[8.0] versus [3.6]–[4.6] color-color diagram of the point sources detected with signal-to-noise ratio better than 5 (photometric error less than 0.2 mag). The boundaries of Class 0/I – III regimes are adopted from Allen et al. (2004).
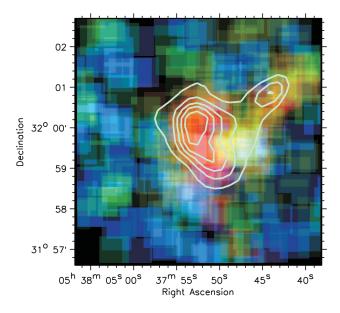

Fig. 6 Pseudo-color image representing the distribution of YSOs in the field. Red represents the Type 1 SED objects; yellow Types 2 and 3; green for Type 4 and blue for Type 5 (see text). The solid contours are a SCUBA 850 μm continuum image (Di Francesco et al. 2008; Klein et al. 2005).

In Figure 6 we overlay the 850 μm contours (Di Francesco et al. 2008)[3] on the image of the YSO distribution. Interestingly, the red peaks coincide with the 850 μm continuum peaks (Klein et al.

---

[3] The 850 μm image can be downloaded at *http://www1.cadc-ccda.hia-iha.nrc-cnrc.gc.ca/community/scubalegacy/*.

2005) very well. This shows that the mm continuum emission is associated with the very young population there. This result confirms our previous conclusion that a cluster with two subgroups is just forming. Taking the NIR cluster into consideration, the whole region shows a star forming sequence where the NIR cluster forms first, and the expanding shell surrounding the NIR cluster may trigger another round of star formation in the NH$_3$ and northwest areas.

Using the JCMT archive data, which were obtained by Di Francesco et al. (2008), and assuming optically thin dust emission, a dust temperature of 20 K, gas-to-dust ratio of 100, grain size of 0.1 μm, grain mass density of 3 g cm^{-3} and a grain emissivity index of 2 (corresponding to $\kappa \approx 0.3$ for comparison with Ossenkopf & Henning 1994), we adopt the equations outlined in Hildebrand (1983) and Beuther et al. (2005) to estimate the gas masses. The final values are ~ 1100 $M_\odot$ and ~ 150 $M_\odot$ in the NH$_3$ core and northwest region, respectively. Meanwhile, the masses of the stellar contents are estimated by SED fittings to be ~ 240 $M_\odot$ and ~ 50 $M_\odot$, respectively. The overall star formation efficiencies are then $\sim 18\%$ and $\sim 25\%$ in these two subregions.

4 CONCLUSIONS

We have carried out a deep observation of the star forming region AFGL 5157 using the Spitzer/IRAC. PAH emissions are found to be extended throughout the field. No destruction of PAH emissions suggests that there are no very high mass stars in the region. The images in the four channels reveal a large number of point sources that are not detected in the NIR. By analyzing the SEDs of the point sources in the NIR and four IRAC channels, we have identified a deeply embedded cluster, which is split into two subgroups. These two subgroups contain a number of point sources with SEDs increasing toward longer wavelengths. They congregate toward the 850 μm continuum peaks (Di Francesco et al. 2008; Klein et al. 2005). The spatial coincidence between the SED I sources and the sub-mm peaks suggests that a new cluster is just forming there. The star formation efficiencies in the two subregions are estimated to be $\sim 18\%$ and $\sim 25\%$, respectively.

In the two subregions, we detected a large number of objects with enhanced emission in ch2. Some of them have counterparts in the NIR H$_2$ narrow band image (Chen et al. 2003), but others do not. We have identified several bipolar jets in the NH$_3$ core region; two of them are associated with CO bipolar outflows. The SED fittings and jet kinematics both suggest that their driving sources are very young. One of the driving sources is not detected even in the IRAC images, but shows faint mm continuum emissions (Fontani et al. 2009). It has probably just started the formation process. Two jets that presumably originated from the northwest region are detected. The widespread H$_2$ knots also support our conclusion that a cluster formed recently.

References

Allen, L. E., Calvet, N., D'Alessio, P., et al. 2004, ApJS, 154, 363

Beuther, H., Schilke, P., Menten, K. M., et al. 2005, ApJ, 633, 535

Canto, J., & Raga, A. C. 1991, ApJ, 372, 646

Chen, Y., Yao, Y., Yang, J., et al. 1999, AJ, 117, 446

Chen, Y., Yao, Y., Yang, J., Zeng, Q., & Sato, S. 2003, A&A, 405, 655

Cyganowski, C. J., Whitney, B. A., Holden, E., et al. 2008, AJ, 136, 2391

Di Francesco, J., Johnstone, D., Kirk, H., MacKenzie, T., & Ledwosinska, E. 2008, ApJS, 175, 277

Fontani, F., Caselli, P., Bourke, T. L., Cesaroni, R., & Brand, J. 2008, A&A, 477, L45

Fontani, F., Zhang, Q., Caselli, P., & Bourke, T. L. 2009, A&A, 499, 233

Hildebrand, R. H. 1983, QJRAS, 24, 267

Klein, R., Posselt, B., Schreyer, K., Forbrich, J., & Henning, T. 2005, ApJS, 161, 361

Kumar, M. S. N., Keto, E., & Clerkin, E. 2006, A&A, 449, 1033

Kumar Dewangan, L., & Anandarao, B. G. 2010, MNRAS, 402, 2583

Molinari, S., Pezzuto, S., Cesaroni, R., et al. 2008, A&A, 481, 345

Ossenkopf, V., & Henning, T. 1994, A&A, 291, 943

Pirogov, L. 1999, A&A, 348, 600

Povich, M. S., Stone, J. M., Churchwell, E., et al. 2007, ApJ, 660, 346

Raga, A., & Cabrit, S. 1993, A&A, 278, 267

Robitaille, T. P., Whitney, B. A., Indebetouw, R., & Wood, K. 2007, ApJS, 169, 328

Snell, R. L., Huang, Y.-L., Dickman, R. L., & Claussen, M. J. 1988, ApJ, 325, 853

Torrelles, J. M., Eiroa, C., Miranda, L. F., et al. 1992, ApJ, 384, 528

Zhang, Q., Hunter, T. R., Brand, J., et al. 2005, ApJ, 625, 864